Emulsion droplet formation in coflowing liquid streams

Yongping Chen,[1,2,*] Liangyu Wu,[2] and Chengbin Zhang[2]

[1]*School of Energy and Power Engineering, Yangzhou University, Yangzhou, Jiangsu 225127, People's Republic of China*

[2]*Key Laboratory of Energy Thermal Conversion and Control of Ministry of Education, School of Energy and Environment, Southeast University, Nanjing, Jiangsu 210096, People's Republic of China*

(Received 20 May 2012; revised manuscript received 4 November 2012; published 3 January 2013)

We investigate emulsion droplet formation in coflowing liquid streams based on a computational fluid dynamics simulation using the volume-of-fluid method to track the interface motion with a focus on the dynamics of the dripping and jetting regimes. The simulations reproduce dripping, widening jetting and narrowing jetting simultaneously in a coflowing microchannel in agreement with the experimental observations in this work. The result indicates that the dripping regime, rather than the jetting regime, is a favorable way to producing monodisperse emulsions. We find that, in dripping and widening jetting regimes, the breakup of a drop is induced by higher pressure in the neck which squeezes liquid into the lower-pressure region in subsequent and primary droplets, while the breakup in the narrowing jetting regime is due to slow velocity at the back end of the trough with respect to the leading end of the trough. In addition, the capillary number of the outer fluid and the Weber number of the inner fluid not only determine the drop diameter and generation rate but also the regime of emulsification.

DOI: 10.1103/PhysRevE.87.013002 PACS number(s): 47.61.Ne, 47.55.dk, 83.50.Ax

I. INTRODUCTION

Emulsification is an important process in both materials science (including the food, pharmaceutical, cosmetics, and chemical industries) and lab on a chip where drops are viewed as microreactors [1–7]. The conventional emulsification techniques often involve mixing of two liquids in bulk processes and under turbulent regimes in order to enhance the breakup of drops. Emulsification through such approaches has proved complicated, and especially high polydispersity has up to now prevented the widespread use of this technique. In the context of this particular situation, microfluidics, a way for producing droplets in a manipulated and reproducible manner, has been developed and has been of considerable interest in the past decade [8–13].

To actively control the droplet production via microfluidics, it is of significance to fully understand the drop formation. There have been several earlier experimental attempts to prepare emulsions by general design of microfluidic devices, including the use of coflowing stream, T junction, and flow focusing [14–16]. Based on these approaches, the droplet formation affected by physical parameters, such as the flow rate of both liquids, their viscosities, interfacial tension, and microchannel geometry, has been examined experimentally [17–19]. It is observed that the dripping regime and the jetting regime (including narrowing jetting and widening jetting) occur in coflowing liquid streams, and the dripping-to-jetting transition mainly depends on the capillary number of the outer fluid and the Weber number of the inner fluid [20]. Both the monodisperse and polydisperse emulsions can be produced by a flow-focusing geometry [16].

Apart from the experimental approaches, theoretical research has also been carried out to investigate drop formation. Now, the interface tracking method and the interface capturing method are the two main numerical approaches to simulate multiphase flow. The boundary-integral method [21–24], finite element method [25–27], and immersed boundary method [28,29] are the typical interface tracking methods, in which the mesh elements lie in part or fully on the interface. For instance, Zhang and Stone [24] studied drop formation at the tip of a vertical circular capillary tube immersed in a second immiscible fluid at low Reynolds number by the use of the boundary-integral method. Wilkes *et al.* [25] used the finite element analyses to simulate the dynamics of drop formation of a Newtonian liquid from a capillary tube into an ambient gas. The interface tracking method is accurate for simulating the onset of breakup and coalescence transitions; however, there are difficulties in simulating through and past the transitions [30]. On the other hand, compared with the interface tracking method, interface capturing methods, such as constrained-interpolation-profile method [31], level set method [32], volume of fluid method [33,34], phase-field method [35], diffuse-interface method [36,37], etc., do not require mesh cut-and-connect operations since the interface evolves through the meshes other than the mesh elements lying on the interface [30]. The emulsification process includes not only the deformation and breakup of the interface but also the movement and development of the interface along with fluid flow which makes the interface capturing method ideal for simulating this immiscible two-phase flow. In addition, the surface tension is generally incorporated into the momentum equation as a source term following the continuum surface force (CSF) model [38]. While under the circumstance of high density ratio, the inconsistent calculation of the interfacial tension force in CSF model can result in the "parasitic currents" [39] phenomenon and may lead to catastrophic instability of the interface or even breakup [34]. However, in our work, only the liquid-liquid multiphase flow with the density ratio of $\rho_i/\rho_o \approx 1$ is considered, hence, the disadvantage of the CSF model under high density ratio is circumvented. Plenty of investigations on multiphase flow using VOF methods can be found [40–44]. Li *et al.* [40] used the VOF method with continuum surface force formulation

*Corresponding author: chenyp@yzu.edu.cn

to investigate the deformation and breakup of a drop in simple shear flow. The comparison between the simulation results and previous experimental data verified the accuracy of the VOF method. Li *et al.* [40] pointed out that the main advantage of the VOF method is its mass conservation property, which makes the rescaling of the mass during the calculation unnecessary, and the other is its ability to compute flows with changes in topology. In addition, compared with the finite element method, the VOF method does not require local mesh refinement in every time step to resolve the interface, which simplifies the treatment of topological changes of the interface and reduces the computational cost. Zhang [41] presented numerical results of the dynamics of a viscous liquid emulsified in another viscous coflowing fluid based on the VOF-CSF method, which is also verified by their experiment photos. As stated by Zhang, the VOF-CSF method allows calculations to pass the breaking point during drop formation continuously without numerical modifications to overcome the singular nature of the interface rupture, which makes it efficient to predict the rheological characteristics of fluid-fluid flow in a coflowing system.

However, the available computational fluid dynamics (CFD) simulations rarely considered the jetting regimes for the viscous liquid drops injected in another immiscible flowing liquid in microfluidic devices. Considering that the deformation of jetting is an unsteady-state process accompanied with complicated interface movement, a question arises as to whether a CFD simulation method can predict the dripping, narrowing jetting and widening jetting simultaneously in a coflowing liquid stream as the experiment observes. The theoretical understanding of the underlying physics of how the breakup of dripping, narrowing jetting and widening jetting occurs in microfluidic devices is still waiting to be explored. In particular, the liquid-liquid interaction and the velocity and pressure distributions at the interface, which can visually demonstrate the dynamics of narrowing jetting and widening jetting, are less understood. For these reasons, here we conduct CFD simulations to investigate droplet formation in coflowing liquid streams, especially in an effort to offer a theoretical prediction for emulsion droplet formation and elucidate the flow regimes of narrowing jetting and widening jetting. In addition, we also conduct the experiment on drop formation in a coflowing liquid stream to give a comparison and validation for the simulation results.

II. MATHEMATICAL MODEL

In order to theoretically predict the emulsion droplet formation and elucidate the flow regimes, we develop a two-dimensional axisymmetric mathematical model for a liquid fed through a nozzle into a coflowing bath of another liquid. As shown in Fig. 1, the coflowing microchannel is made of two coaxially aligned capillary channels, and the incompressible dispersed phase (Newtonian, oil, density ρ_o, viscosity μ_o) injects at a constant flow rate, q_i, into an immiscible, incompressible continuous phase (Newtonian, water, ρ_w, μ_w) at the tip of the inner capillary channel. The external liquid water with a constant flow rate, q_o, exerts pressure and viscous stresses that force the oil into a narrow thread, and then the oil breaks into drops nearby or downstream.

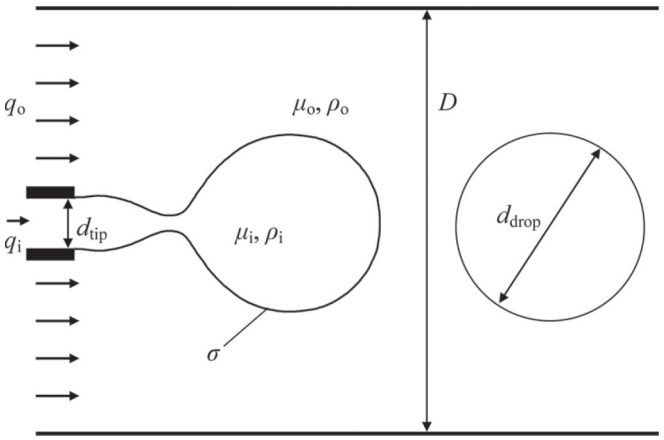

FIG. 1. Schematic of droplet formation in coflowing microchannel.

To study the dynamics of droplet formation numerically, the VOF method is utilized in the CFD simulations to describe the positions and motions of the liquid-liquid interfaces. The portion of the two fluids in a computational cell is represented by the volume fraction α:

$\alpha = 1$, the cell is filled with fluid 1;

$\alpha = 0$, the cell is filled with fluid 2;

$0 < \alpha < 1$, the cell contains the interface.

In each control volume, the volume fractions of all phases sum up to unity,

$$\alpha_o + \alpha_i = 1, \tag{1}$$

where α_i and α_o represent the volume fractions of the oil and water phases.

In this paper, tracking and locating the interfaces is accomplished by solving a single set of continuity equations for the volume fractions of oil phase, α_i,

$$\frac{\partial \alpha_i}{\partial t} + \vec{U} \cdot \nabla \alpha_i = 0 \tag{2}$$

where t is the time and $\vec{U}$ is the velocity vector governed by the mass and momentum equations for incompressible Newtonian fluid:

$$\nabla \cdot \vec{U} = 0, \tag{3}$$

$$\frac{\partial \vec{U}}{\partial t} + \nabla \cdot (\vec{U}\,\vec{U}) = -\frac{\nabla p}{\rho} + \frac{\mu}{\rho} \nabla \cdot [\nabla \vec{U} + \nabla \vec{U}^T] + f, \tag{4}$$

where p is the pressure, and ρ and μ are the density and viscosity interpolated as

$$\rho = \alpha_i \rho_i + (1 - \alpha_i)\rho_o, \tag{5}$$

$$\mu = \alpha_i \mu_i + (1 - \alpha_i)\mu_o. \tag{6}$$

And $f = g + f_{sv}$ is the source term including gravity, g, and the interfacial tension force, f_{sv}. Since the length scale is micrometer, gravity is negligible. While the interfacial tension is introduced following the continuum surface force (CSF) scheme [38]:

$$f_{sv} = \sigma \kappa \hat{n} \delta_s, \tag{7}$$

where σ is the interfacial tension coefficient, κ is the mean curvature of the interface, $\hat{n}$ is the unit normal to the interface, and δ_s is the interface delta function. Besides, the surface normal of those cells at the wall is determined by the contact angle, θ, between the interface and the wall by

$$\hat{n} = \hat{n}_w \cos\theta + \hat{t}_w \sin\theta, \tag{8}$$

where $\hat{n}_w$ and $\hat{t}_w$ are the unit vectors normal and tangential to the wall, respectively. If not specified, the results reported in this paper are obtained with the contact angle of 120°. Note that the viscous dissipation and the enthalpy change are considered negligible in the model. Such neglect is usually applied in previous studies of a viscous liquid ejected into another immiscible viscous coflowing fluid [24,41,42].

III. NUMERICAL SOLUTION

The numerical solution is performed using a commercial CFD code, FLUENT 6.2, which is a vertex-centered code based on the finite volume method. In the simulation, the laminar model is applied to simulate the liquid flow during the drop formation. The pressure-velocity coupling is obtained by the semi-implicit method for pressure linked equations (SIMPLE) algorithm. A second-order upwind scheme is employed to discretize the momentum equation. The piecewise linear interface calculation (PLIC) [44] interface reconstruction technique is used to track the geometry of the interface in all cases simulated. The evolution of the flow pattern is tracked by a transient simulation. A variable time step scheme is implemented to reduce the computational cost under the criterion that the global Courant number (a dimensionless number that compares the time step to the characteristic time of transit of a fluid element across a control volume) is less than 0.5. As the convergence criterion, the sum of the normalized relative residuals in each control volume for all the variables are controlled to be less than 0.1% in a time step. The simulation test indicates that a good convergence is reached if the under-relaxation factors are used at these values: 0.1 (pressure), 0.1 (density), 0.1 (body force), 0.8 (momentum). The calculations are performed by a work station with 8 2.0 GHz processors and 8.0 GB of RAM. Depending on different cases, the computational time varies from a couple of hours to two days.

As shown in Fig. 2, a grid sensitivity study is conducted using three kinds of grid size: coarse grid (11 320 grids), medium grid (19 425 grids), and fine grid (24 075 cells). Comparison of the three cases showed that the latter two cases do not generate a noticeable difference in interface shape under the same parameters and operating conditions. Considering the computer system configuration and results of the calculations, the medium grid was used in this study to ensure that acceptable results could be obtained with reasonable computational time.

IV. EXPERIMENTAL VERIFICATION

As shown in Fig. 3, a coflowing stream is implemented on a microfluidic device with a steel needle inserted inside a rectangular channel fabricated on a polyamides brick. The needle is located in the middle of the cross section of a

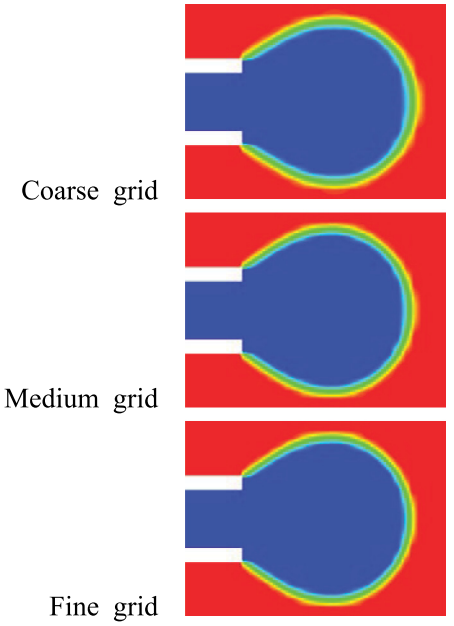

FIG. 2. (Color online) Simulation results for grid sensitivity study at $t = 0.001$ s.

rectangular channel and is parallel to the channel so as to obtain an axisymmetric flow. The dispersed phase is injected via the steel needle and the continuous phase is injected through the channel. The dispersed and continuous phases are delivered respectively by a syringe pump at a specific flow rate. In the experiment, silicon oil is dispersed in a continuous phase of de-ionized water and sodium dodecyl sulfate (SDS) is added to water to adjust the interfacial tension. The drop formation in the coflowing liquid streams is recorded by a microscope (Zoom 160 optical system) and a high-speed video camera

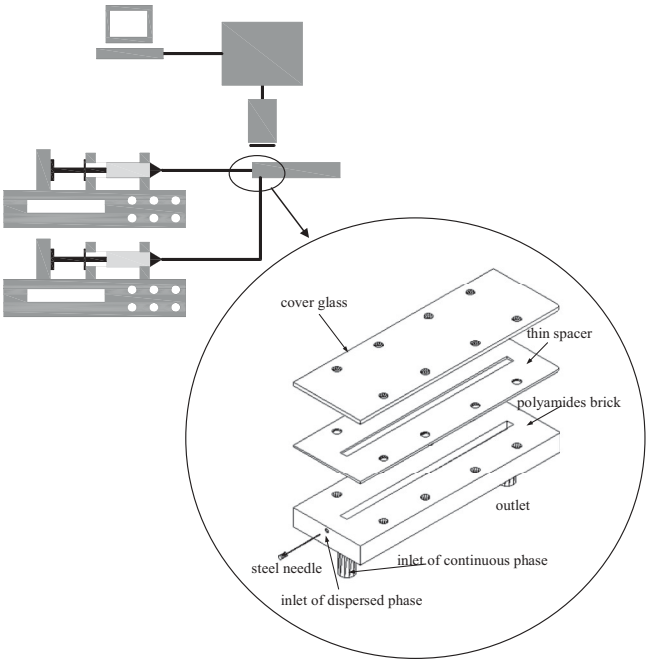

FIG. 3. Experimental setup of droplet formation in coflowing microchannel.

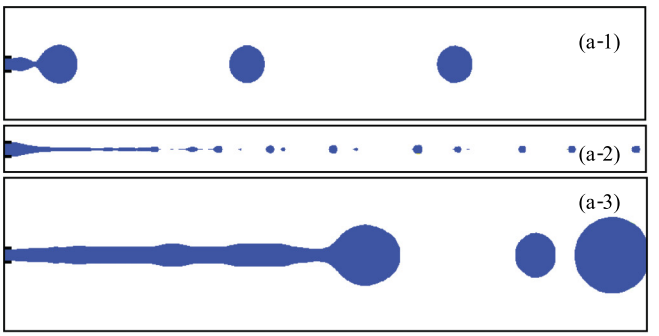

(a)

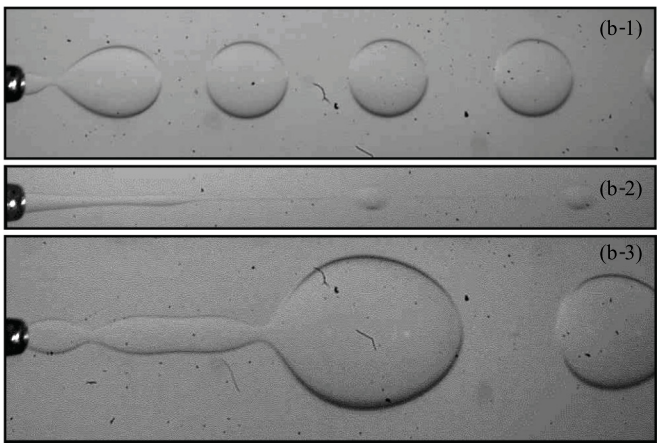

(b)

FIG. 4. (Color online) Flow regimes of droplet formation in coflowing microchannel: (a) Numerical result, and (b) experimental images.

(Photron SA4) which captures up to 500 fps at a full resolution of 1024 × 1024 pixels.

Using the mathematical model of drop formation in a coflowing microchannel as stated above, a wide range of variations in the flow rates, viscosity ratio, and interfacial tension are examined in the simulation to study the drop formation in coflowing liquid streams. The simulations reproduce two typical regimes governing the drop formation flow patterns, dripping and jetting (including narrowing jetting and widening jetting), as shown in Fig. 4(a), which agrees with experimental observation [see Fig. 4(b)] in a coflowing microchannel obtained in this work. The agreement verifies that the present model is reasonable, and CFD simulation is capable of predicting the dripping, narrowing jetting and the widening jetting drop formation simultaneously.

V. RESULTS AND DISCUSSION

A. Dripping regimes

As stated by Utada *et al.* [20], dripping is a common case in drop formation with individual drops detaching from the tip periodically and constantly. It occurs at low flow rates of both fluids, as shown in Figs. 4(a-1) and 4(b-1). Figure 5 provides a complete view of typical dripping. The drop formation process under the dripping regime is usually divided into two stages: growth and separation. At the earlier

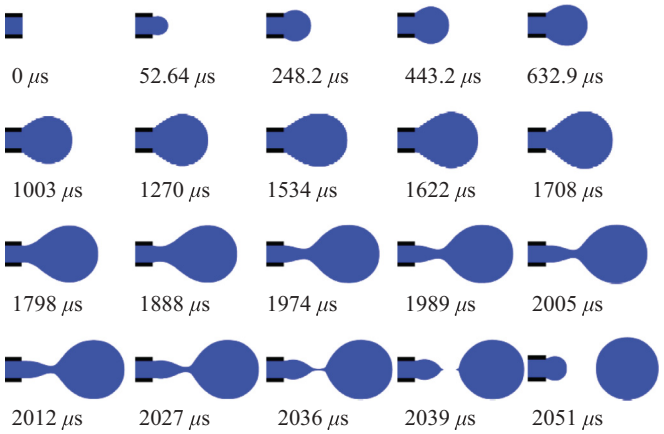

FIG. 5. (Color online) A time sequence of dripping regime ($\lambda = 10$, $Ca_o = 0.08$, $We_i = 0.05$).

stage of growth ($t \leqslant 632.9$ μs), the drop volume increases due to the continuous addition of inner fluid and the interface shape remains essentially spherical as the interfacial tension dominates. As the inner fluid injects into the primary drop, the velocity of the inner fluid decreases while the surface area of the primary drop grows, which implies that the kinetic energy of the inner fluid transforms into the surface energy of the primary drop to enlarge the surface area. Later, with drop size increasing, the viscous drag of ambient liquid becomes comparable to its opposite force (i.e., the interfacial tension); the local vortex motion near the liquid-liquid interface inside the drop [see inset in Fig. 6(a)] develops, which stretches the drop along the flow direction and transforms it slowly from spherical to pear shaped (e.g., 1003 μs in Fig. 5) and brings out the formation of a neck between the drop and the tip (e.g., 1708 μs in Fig. 5). Once a visible neck emerges, the drop formation process begins coming into the separation stage (1798–2039 μs), during which the drop reaches a critical volume and the breakup occurs. At the time $t = 1798$ μs, the neck has nearly the same size as the inner diameter of the tip. Then, under external viscous flow, the part of the neck which is close to the almost spherical drop narrows quickly. Decreases in the diameter of the neck with time caused by local interfacial tension [e.g., 2027 μs in Fig. 6(b)] lead to a high-pressure region. The high-pressure region squeezes the liquid in the neck towards the low-pressure region [e.g., 2036 μs in Fig. 6(b)] in the primary droplet and subsequent droplet (i.e., olive-shaped droplet). At this time, due to the competition between the interface tension and viscous drag for the droplet attached to the tip (called the olive-shaped droplet), the inner fluid along with the ambient fluid develops a local vortex at the front edge of the olive-shaped droplet. The vortex flow pushes the olive-shaped droplet moving back towards the tip at $t = 2039$ μs as shown in Fig. 6(b). This movement accelerates the narrowing of the neck and eventually breakup occurs at $t \approx 2039$ μs producing a single spherical droplet with a single olive-shaped drop remaining attached to the tip. Trails exist between two newly formed droplets and are soon retracted due to local interfacial tension. After a complete formation process, the subsequent droplet attached to the tip continues to deform and subsequently develops another similar drop formation behavior. In the dripping case, the generated

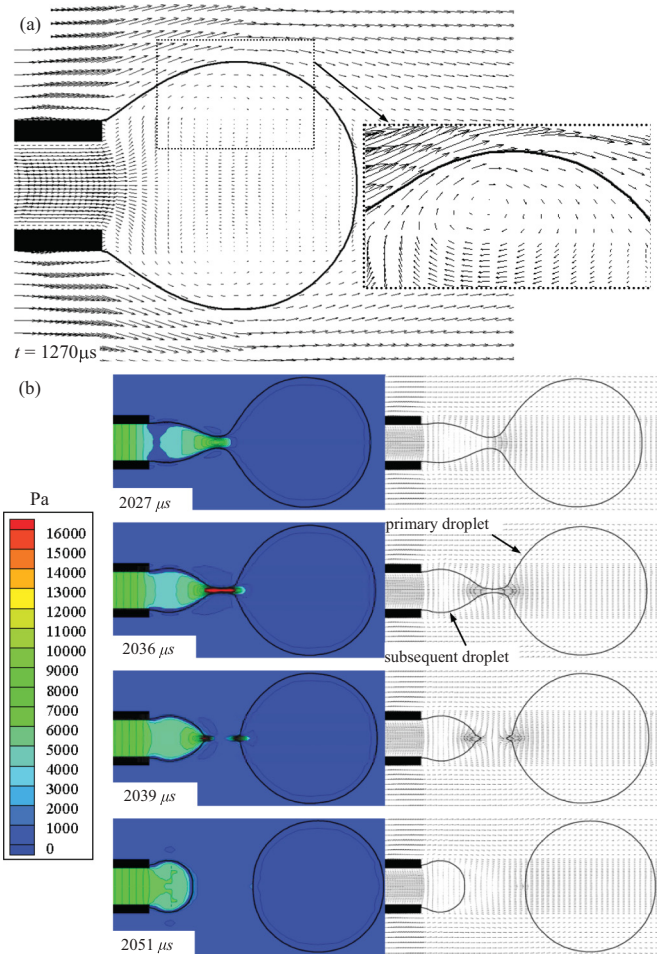

FIG. 6. (Color online) Pressure and velocity profile for dripping regime ($\lambda = 10$, $Ca_o = 0.08$, $We_i = 0.05$): (a) Local velocity field, and (b) local pressure and velocity profile.

droplets are almost of the same size, so it is an efficient way to produce monodisperse emulsions.

B. Jetting regimes

Jetting is another type of regime governing the drop formation with an injected liquid stream that breaks into droplets away from the tip [20]. Jetting occurs at fast flows of either fluid and exhibits two distinct types. In the case of increasing the flow rate of outer fluid, the droplets are generated at the leading end of the jet and narrowing jetting appears [see Figs. 4(a-2) and 4(b-2)]. The other type of jetting is driven by the increasing of the flow rate of the inner fluid. A jet with a bulbous end widening downstream appears and the breakup of drops also occurs at the leading end of the jet [see Figs. 4(a-3) and 4(b-3)]. Unlike dripping, both jetting cases are unstable, either accompanied by satellite drops after drop formation or alternating drops with large and small sizes.

Figure 7(a) illustrates a time sequence of typical narrowing jetting, which produces droplets with the approximate size of the inner diameter of the tip. It can be observed that the jet does not form instantaneously. The flow condition is similar to dripping at an early stage since interfacial tension dominates initially, and the difference consists in a smaller bulbous end. When the viscous force is comparable to the interfacial

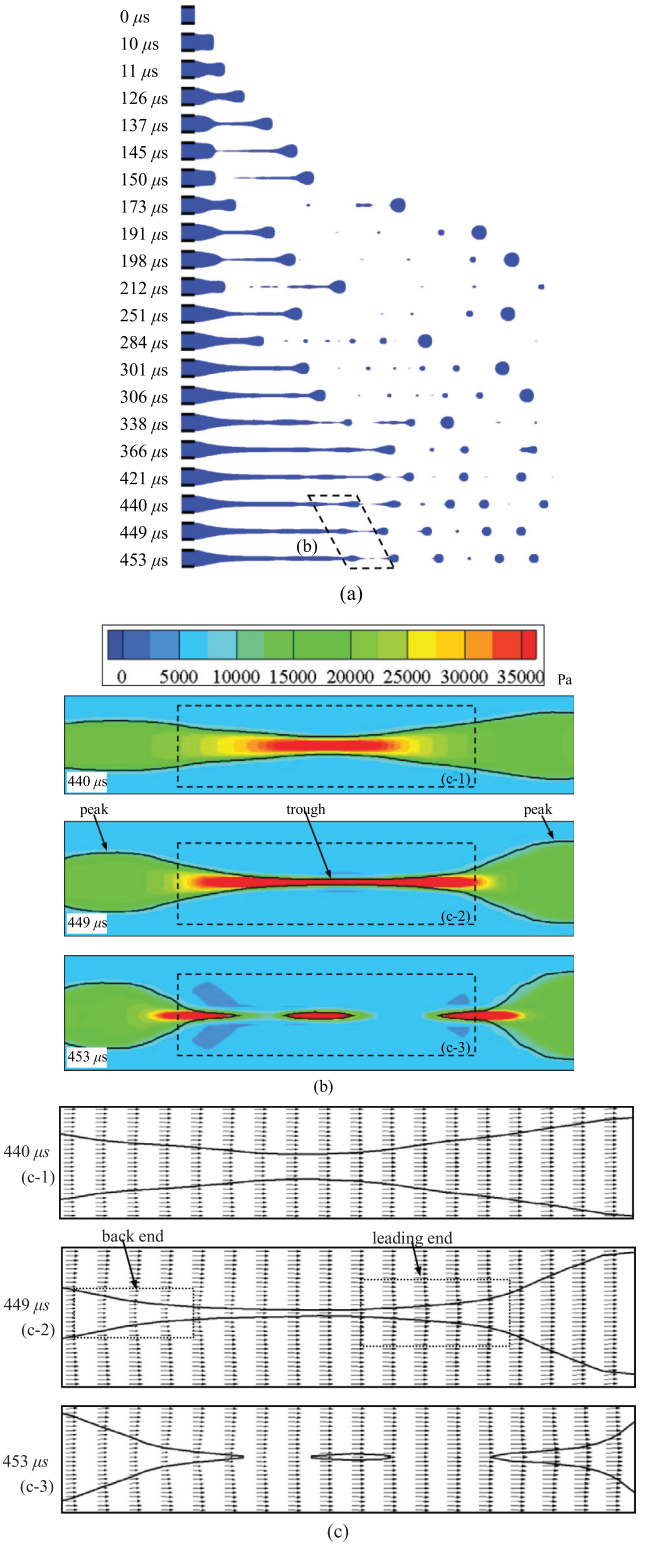

FIG. 7. (Color online) A typical narrowing jetting case ($\lambda = 10$, $Ca_o = 0.85$, and $We_i = 0.08$): (a) Time sequence, (b) local pressure profile at the instant of breakup of the trough, and (c) local velocity profile at the instant of breakup of the trough.

tension, the liquid-liquid interface develops undulations while the neck of the drop is stretched and the jet occurs. In this process, the position of jetting moves downstream and

the droplet diameter of the jetting decreases and ultimately reaches a roughly constant value. It is important to note that, in the narrowing jetting, the formation and breakup of a single droplet appears downstream and satellite droplets with smaller magnitude accompany almost every droplet. Therefore, the narrowing jetting is not a favorable way to produce monodisperse emulsions owning to the unequal size of the droplets.

In order to analyze how the narrowing jetting occurs, Figs. 7(b) and 7(c) depict the transient distributions of pressure and velocity in and around the drop. As shown in the figure, the radius of the drop is smaller at the trough and a higher pressure is induced in the trough due to the surface tension, which acts as an internal force toward the lower-pressure region in the peak. Under the coupled effects of viscous drag of the outer fluid and surface tension, the velocity components at the leading end of the trough grow with time while those at the back end of trough decay with time. The nonuniform velocity distributions imposed on the drop narrow the trough of the undulation and finally pinch the stream into droplets. In addition, since the viscous drag dominates the formation and breakup of the drop, there is no obvious retraction of inner fluid after pinching-off and also no vortex motion around the pinching point.

The widening jetting, as shown in Fig. 8(a), is characterized by a jet which is widening and undulating during the formation of the primary drop. In this type of jetting, the inertial force of the inner fluid becomes large enough to push the drop downstream and the primary drop grows when pushed downstream. The subsequent drop just begins to grow at the end of the jet. A large shear at the interface, which is opposite to the flow direction of the inner fluid, decelerates the jet, causing the front end of the drop to be widened. Differing from narrowing jetting, the pinching-off of drops under this jetting mode is somewhat similar to dripping. The droplets are bigger than the diameter of the tip and are rarely accompanied by satellite drops. The diverse droplet sizes are observed in the widening jetting regime [see Fig. 4(a-3)], so it is also not a favorable way to produce monodisperse emulsions.

Figure 8(b) presents the transient distributions of pressure and velocity in and around the drop at the instant of drop breakup. From the figure, we can get some information on how the widening jetting occurs. The diameter of the neck is far smaller than that of the primary drop, which contributes to a larger pressure in the neck owing to the surface tension. Additionally, the velocity in the neck is larger than that of the surrounding fluid, including the outer fluid, primary drop, and subsequent drop [see 15 010 μs in Fig. 8(b)]. With a decrease in neck diameter, a sufficiently large pressure is induced and squeezes liquid into the lower-pressure region in both primary drop and subsequent drop [see 15 060 μs in Fig. 5(b)]. As time progresses, the neck pinches off and generates the primary drop. It is also indicated that vortex formation occurs at the front of the subsequent drop when the liquid in the neck is squeezed into the lower-pressure region, and a slight retraction at the end of the jet after pinching-off is observed (e.g., $t = 15\,080$ μs).

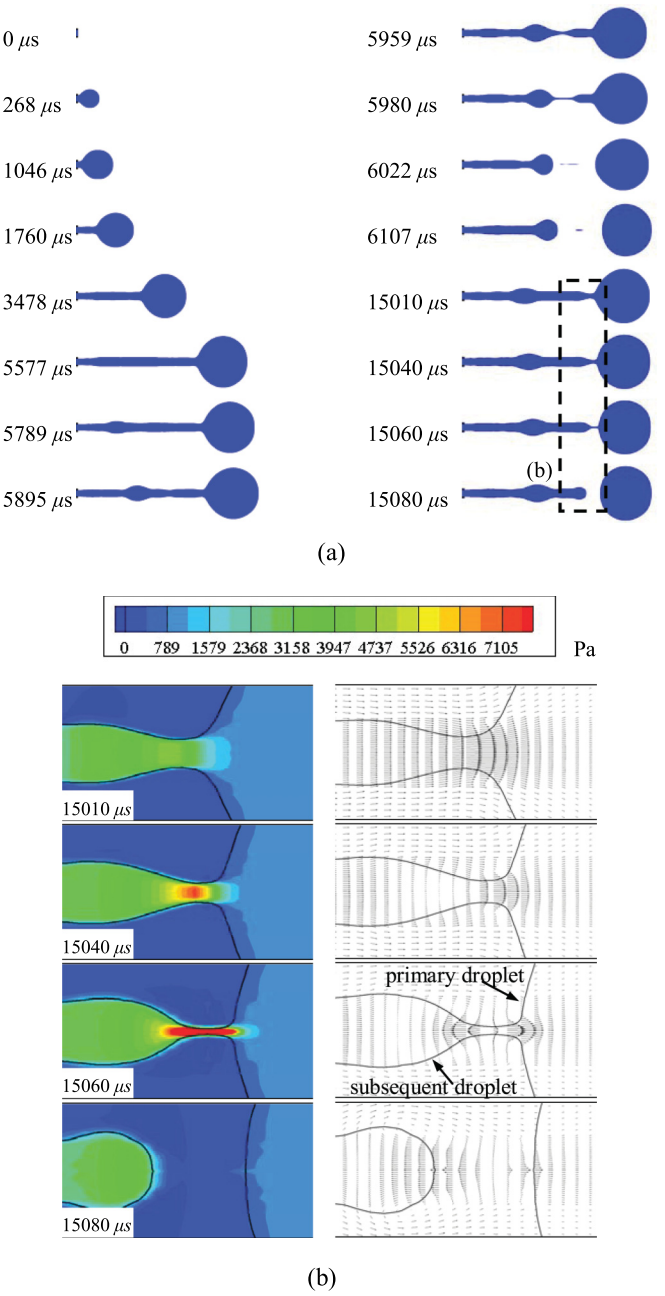

FIG. 8. (Color online) A typical widening jetting case ($\lambda = 10$, $Ca_o = 0.02$, and $We_i = 1.60$): (a) Time sequence, (b) local pressure and velocity profile.

C. Influence factors analysis

In order to analyze the influence of flow parameters on the emulsion droplet formation in coflow microfluidic systems, here, two evaluation criteria, the dimensionless drop diameter $d^* = d_{drop}/d_{tip}$ and the generation rate f are introduced, in which d_{drop} is the statistical average diameter of drops, d_{tip} is the inner diameter of the inner tube, and f represents the statistical average number of drops generated in 1 s.

The viscosity ratio between the dispersed phase and continuous phase plays a significant role in the dynamic processes of drop formation, especially the necking and detaching. Figure 9(a) illustrates the interface shapes with different viscosity ratio at the instant of pinching-off of the primary droplet and the variation of d^* and f versus λ. Obviously, as λ increases, a longer neck develops and the primary drop

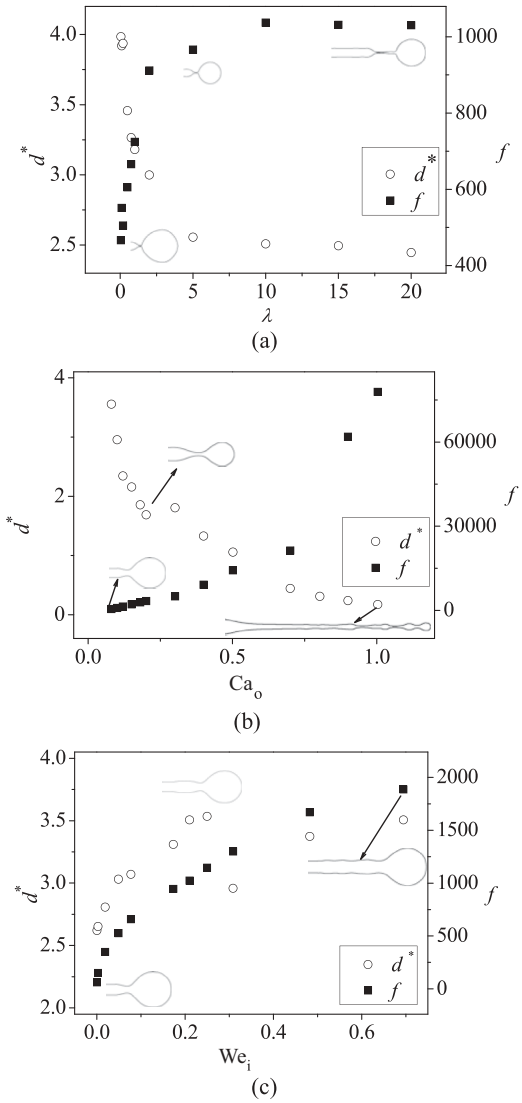

FIG. 9. Dependency of generation rate and drop diameter on physical parameters: (a) Viscosity ratio ($q_i = 90\,\mu$L/h, q_o = 9 mL/h, and $\mathrm{We}_i = 0.003$), (b) capillary number of outer fluid ($\mathrm{We}_i = 0.003$, $\lambda = 10$), and (c) Weber number of inner fluid ($\mathrm{Ca}_o = 0.02$, $\lambda = 1$).

tends to shrink. This trend corresponds with the simulation results presented by Zhang and Stone who investigated the drop deformation in viscous flow at a vertical capillary tube with external free boundary condition [24]. For $\lambda < 1$, the outer fluid is more viscous than the inner one, which leads to slower momentum transfer from the inner fluid to the outer and hence prevents the shaping of a long neck. Due to this fact, the formation rate of drops is slower but with bigger drop size. On the contrary, when $\lambda > 1$, the outer fluid is less viscous and momentum transfer is more efficient, and thus the smaller drops are generated leading to a higher generation rate.

Figure 9(b) plots the droplet diameter distribution and its generation rate as a function of the capillary number of the outer fluid, Ca_o (defined as the ratio of viscous force to interfacial tension), which is capable of representing the effect of strain rate during the emulsification processes. As indicated, a sharp jump of the droplet diameter in the vicinity of $\mathrm{Ca}_o \approx 0.3$ is a criterion of flow regime transition. In the case of $\mathrm{Ca}_o < 0.3$ where the drop formation regime is dripping, the droplet diameter d^* decreases significantly with increasing Ca_o, and the generation rate f is insensitive to the Ca_o. However, in the case of $\mathrm{Ca}_o > 0.3$ where the narrowing jetting is the governing drop formation regime, the drop diameter decreases slowly with Ca_o and can be even smaller than that of the tip. Additionally, a drastic increase appears in the generation rate with increasing Ca_o since satellite drops accompany almost every droplet in the narrowing jetting. The correlation between the droplet diameter and Ca_o can be expressed as $d = 4.4e^{-2.79\mathrm{Ca}_o} - 0.093$ ($\mathrm{Ca} < 0.3$) and $d = 14.09e^{-25.97\mathrm{Ca}_o} + 1.8$ ($\mathrm{Ca} > 0.3$) for dripping and jetting domain, respectively.

Figure 9(c) represents the effect of the Weber number of the inner fluid on droplet diameter and its generating rate. As shown in the figure, a sharp dive of droplet diameter at $\mathrm{We}_i \approx 0.2$ is induced by the transition from dripping regime to widening jetting regime. In dropping regime or widening jetting regime, the droplet diameter and generating rate increases monotonically with the increasing We_i.

VI. CONCLUSION

In this paper, the growth, extension, and breakup of an ejected liquid drop under external viscous liquid forced flow in a coflowing microchannel is investigated by CFD simulation with VOF representation of the interface. The simulation reproduces the flow regimes, including the dripping, widening jetting and the narrowing jet, in agreement with the experimental observations of this work and visually demonstrates the dynamics of dripping and jetting regimes. The effects of the viscosity ratio, capillary number, and Weber number on drop formation dynamics are presented. We find that in dripping and widening jetting regimes, the breakup of the drop is induced by higher pressure in the neck which squeezes liquid into the lower-pressure region in subsequent and primary droplets, while the breakup in the narrowing jetting regime is due to slow velocity at the back end of the trough with respect to the leading end of the trough. In particular, the vortex motion occurs owing to surface tension in and around the subsequent droplet during the breakup of the drop in dripping and widening jetting regimes, however, no vortex motion is observed in the narrowing jetting regime. In addition, the capillary number of the outer fluid and the Weber number of the inner fluid not only determine the drop diameter and generation rate but also the regime of emulsification, and the dropping regime, rather than jetting regime, is a favorable way to produce monodisperse emulsions.

ACKNOWLEDGMENT

This work was supported by National Natural Science Foundation of China (Grant No. 51222605) and Natural Science Foundation of Jiangsu Province (Grant No. BK2011062).

[1] M. Windbergs and D. A. Weitz, Small **7**, 3011 (2011).
[2] S. S. Datta, D. D. Gerrad, T. S. Rhodes, T. G. Mason, and D. A. Weitz, Phys. Rev. E **84**, 041404 (2011).
[3] S. Seiffert and D. A. Weitz, Polymer **51**, 5883 (2010).
[4] K. J. Humphry, A. Ajdari, A. Fernández-Nieves, H. A. Stone, and D. A. Weitz, Phys. Rev. E **79**, 056310 (2009).
[5] P. Poulin and D. A. Weitz, Phys. Rev. E **57**, 626 (1998).
[6] H. Song, D. L. Chen, and R. F. Ismagilov, Angew. Chem. **45**, 7336 (2006).
[7] C. N. Baroud, F. Gallaire, and R. Dangla, Lab Chip **10**, 2032 (2010).
[8] D. R. Link, S. L. Anna, D. A. Weitz, and H. A. Stone, Phys. Rev. Lett. **92**, 054503 (2004).
[9] G. F. Christopher and S. L. Anna, J. Phys. D: Appl. Phys. **40**, R319 (2007).
[10] K. Ahn, J. Agresti, H. Chong, M. Marquez, and D. A. Weitz, Appl. Phys. Lett. **88**, 264105 (2006).
[11] H. Kim, D. W. Luo, D. Link, D. A. Weitz, M. Marquez, and Z. D. Cheng, Appl. Phys. Lett. **91**, 133106 (2007).
[12] R. K. Shah, H. C. Shum, A. C. Rowat, D. Lee, J. J. Agresti, A. S. Utada, L. Y. Chu, J. W. Kim, A. Femandaz-Nieves, C. J. Martinez, and D. A. Weitz, Materials Today **11**, 18 (2008).
[13] A. R. Abate, A. Rotem, J. Thiele, and D. A. Weitz, Phys. Rev. E **84**, 031502 (2011).
[14] P. B. Umbanhowar, V. Prasad, and D. A. Weitz, Langmuir **16**, 347 (2000).
[15] T. Thorsen, R. W. Roberts, F. H. Arnold, and S. R. Quake, Phys. Rev. Lett. **86**, 4163 (2001).
[16] S. L. Anna, N. Bontoux, and H. A. Stone, Appl. Phys. Lett. **82**, 364 (2003).
[17] T. M. Squires and S. R. Quake, Rev. Mod. Phys. **77**, 977 (2005).
[18] N. Serra, N. Berton, M. Bouquey, L. Part, and G. Hadziioannou, Langmuir **23**, 7745 (2007).
[19] T. Nisisako, T. Torii, and T. Higuchi, Chem. Eng. J. **101**, 23 (2004).
[20] A. S. Utada, A. Fernandez-Nieves, H. A. Stone, and D. A. Weitz, Phys. Rev. Lett. **99**, 094502 (2007).
[21] A. Z. Zinchenko, M. A. Rother, and R. H. Davis, J. Fluid Mech. **391**, 249 (1999).
[22] V. Cristini, J. Blawzdziewicz, and M. Loewenberg, Phys. Fluids **10**, 1781 (1998).
[23] V. Cristini, J. Blawzdziewicz, and M. Loewenberg, J. Comput. Phys. **168**, 445 (2001).
[24] D. F. Zhang and H. A. Stone, Phys. Fluids **9**, 2234 (1997).
[25] E. D. Wilkes, S. Phillips, and O. Basaran, Phys. Fluids **11**, 3577 (1999).
[26] P. K. Notz, A. U. Chen, and O. A. Basaran, Phys. Fluids **13**, 549 (2001).
[27] J. R. Castrejón-Pita, N. F. Morrison, O. G. Harlen, G. D. Martin, and I. M. Hutchings, Phys. Rev. E **83**, 036306 (2011).
[28] G. Tryggvason, B. Bunner, A. Esmaeeli, D. Juric, N. Al-Rawahi, W. Tauber, J. Han, S. Nas, and Y.-J. Jan, J. Comput. Phys. **169**, 708 (2001).
[29] S. Shin and D. Juric, J. Comput. Phys. **180**, 427 (2002).
[30] V. Cristini and Y. C. Tan, Lab Chip **4**, 257 (2004).
[31] T. Yabe, F. Xiao, and T. Utsumi, J. Comput. Phys. **169**, 556 (2001).
[32] S. Osher and R. Fedkiw, J. Comput. Phys. **169**, 463 (2001).
[33] C. W. Hirt and B. D. Nichols, J. Comput. Phys. **39**, 201 (1981).
[34] D. Gerlach, G. Tomar, G. Biswas, and F. Durst, Int. J. Heat Mass Transf. **49**, 740 (2006).
[35] D. Jacqmin, J. Comput. Phys. **155**, 96 (1999).
[36] D. M. Anderson, G. B. McFadden, and A. A. Wheeler, Annu. Rev. Fluid Mech. **30**, 139 (1998).
[37] P. T. Yue, J. J. Feng, C. Liu, and J. Shen, J. Fluid Mech. **515**, 293 (2004).
[38] J. U. Brackbill, D. B. Kothe, and C. Zemach, J. Comput. Phys. **100**, 335 (1992).
[39] B. Lafaurie, C. Nardone, R. Scardovelli, S. Zaleski, and G. Zanetti, J. Comput. Phys. **113**, 134 (1994).
[40] J. Li, Y. Y. Renardy, and M. Renardy, Phys. Fluids **12**, 269 (2000).
[41] X. G. Zhang, Chem. Eng. Sci. **54**, 1759 (1999).
[42] I. Kobayashi, S. Mukataka, and M. Nakajima, Langmuir **20**, 9868 (2004).
[43] M. Ohta, M. Yamamoto, and M. Suzuki, Chem. Eng. Sci. **50**, 2923 (1995).
[44] D. Gueyffier, J. Li, A. Nadim, R. Scardovelli, and S. Zaleski, J. Comput. Phys. **152**, 423 (1999).